ACS NANO

www.acsnano.org

ARTICLE

Bulk Production of Any Ratio ^{12}C:^{13}C Turbostratic Flash Graphene and Its Unusual Spectroscopic Characteristics

Kevin M. Wyss, Zhe Wang, Lawrence B. Alemany, Carter Kittrell, and James M. Tour*

Cite This: *ACS Nano* 2021, 15, 10542–10552

Read Online

ACCESS | Metrics & More | Article Recommendations | Supporting Information

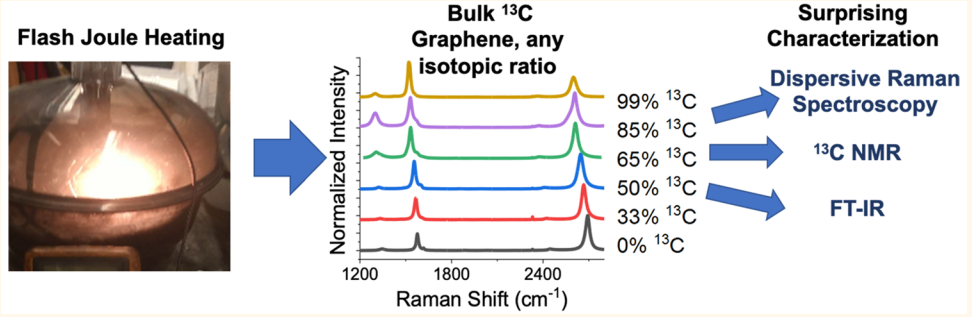

ABSTRACT: **As graphene enjoys worldwide research and deployment, the biological impact, geologic degradation, environmental retention, and even some physical phenomena remain less well studied. Bulk production of ^{13}C-graphene yields a powerful route to study all of these questions. Gram-scale synthesis of high-quality and high-purity turbostratic flash graphene with varying amounts of ^{13}C-enrichment, from 5% to 99%, is reported here. The material is characterized by solid state NMR spectroscopy, Raman spectroscopy, IR spectroscopy, X-ray photoelectron spectroscopy, and inductively coupled plasma mass spectrometry. Notably, an unusual enhancement in the Raman spectroscopic D′ peak is observed, resulting from the modification in vibrational frequency through isotopic enrichment favoring intravalley phonon scattering modes. While the IR absorbance spectrum of graphene is for the most part silent, we prepare here ^{13}C-enhanced graphene samples that show a large aromatic $^{12}C{=}{=}{=}^{13}C$ stretch that reveals this IR-active mode.**

KEYWORDS: *graphene, ^{13}C, turbostratic graphene, Raman spectroscopy, large aromatic $^{12}C{=}{=}{=}^{13}C$ stretch infrared mode*

Graphene is an interesting material, and the field is seeing extensive study with a rapidly growing list of applications. Known for its outstanding physical,[1−3] mechanical,[4−7] and electronic properties,[8−11] the past 16 years has seen an explosion in published and patented applications. Promisingly, the family of graphene nanomaterial nanocomposites show incredible benefits in materials and mechanical properties,[12−15] but graphene and its derivatives have also been implemented in drug delivery,[16] energy storage,[17,18] flexible electronics,[19] and next-generation sensors.[20] As the list of applications grow, and the price of graphene declines, making it more accessible, widespread use is inevitable.[21] Though there is a growing body of literature on the environmental impact, degradation, and toxicity of pristine graphene, to responsibly implement graphene and graphene family nanomaterials, it is essential that we understand their environmental geological fate.

It is important to understand if graphene is biodegradable or bioaccumulated, and if it will generate polyaromatic hydrocarbons (PAH) upon degradation.[22−24] Recent work involves the use of graphene/graphene oxide (GO) and mass spectrometry to study its degradation and biological uptake.[25−27] However, most of these studies are carried out using commercially available graphene, which varies wildly in quality,[28] and some of even the most widely cited studies on graphene toxicity do not adequately characterize the materials used. Graphene has been used that is devoid of the 2D band in

Received: April 15, 2021
Accepted: May 24, 2021
Published: June 7, 2021

https://doi.org/10.1021/acsnano.1c03197
ACS Nano 2021, 15, 10542−10552

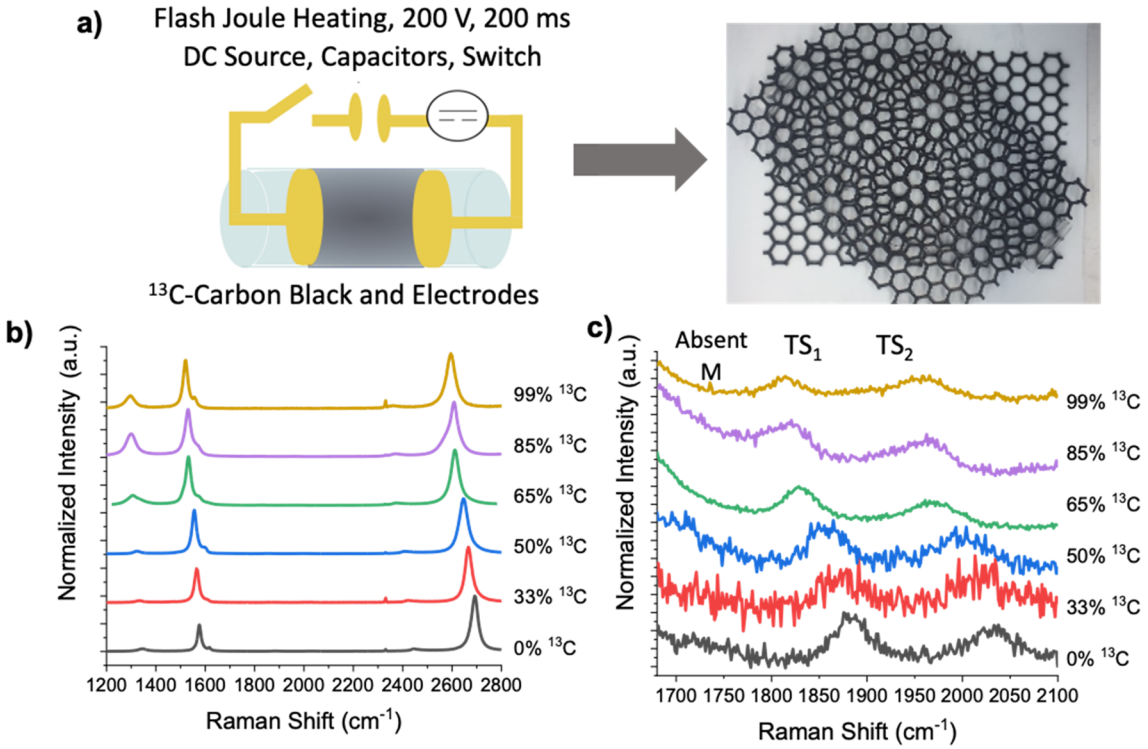

Figure 1. (a) Schematic of the FJH process forming ^{13}C-tFG; (b) representative Raman spectra of tFG enriched with varying concentrations of ^{13}C; (c) Raman spectra showing the TS_1 and TS_2 peaks (1875 and 2025 cm^{-1} in ^{12}C graphene, respectively) in each sample, as well as the notable absence of the M peak (1750 cm^{-1} in ^{12}C graphene).

the Raman spectra,[29] and X-ray photoelectron spectroscopy (XPS) shows the extensive presence of non-carbon elements and trace metals, which can impact conclusions.[30] This makes comparing results and drawing applicable conclusions difficult. There is no literature on the fate of bulk turbostratic graphene even though a recent method to prepare this material could make it the scaled material of choice.[31] Furthermore, the high price of mass production makes large-scale studies difficult. Use of ^{13}C-enriched GO has seen limited use in these applications, and exceedingly little is published on ^{13}C-graphene synthesized through chemical vapor deposition or arc discharge or its applications.[27,32] High-quality, isotopically enriched turbostratic graphene will garner significant interest in biologic, environmental, spectroscopic, conductivity, and phonon physical studies.

Recently, through use of flash Joule heating (FJH), the bulk synthesis of high-quality turbostratic flash graphene (tFG) has been achieved.[33] FJH passes high current through the somewhat resistive material (~1 Ω), generating temperatures in excess of 3000 K within milliseconds. This purifies the carbonaceous starting material through sublimation of non-carbon atoms including Si and Al, as well as rearranging the chemical bonding structure to the enthalpically favored sp^2-carbon-hybridized graphene. Due to the very short duration of heating, the graphene sheets are kinetically trapped in a rotationally disordered (turbostratic) form, producing tFG, as the rapid cooling rate limits crystallization to form AB-stacked graphite. Turbostratic graphene and twisted multilayered graphene are synonymous, with turbostratic graphene being more historical and describing basal planes of a crystal having slipped out of alignment, while twisted multilayered graphene is more commonly used for CVD-grown systems that are not Bernal stacked. We exploit this recent synthetic method to synthesize ^{13}C-enriched graphene and characterize it, with an eye toward future applications in geochemistry, biological, materials science, and 2D physical studies. We envision the widespread use of isotopically enriched tFG in all of these applications and assert that FJH is an accessible technique that permits easy access to bulk quantities for those studies. Finally, the tFG has an unusual enhancement in the Raman spectroscopic D′ band, and the 1:1 ^{12}C:^{13}C sample shows the long-sought C═C stretch in the IR spectrum.

RESULTS AND DISCUSSION

To enrich the ^{13}C-content of the graphene, 99% isotopically pure ^{13}C-carbon black (^{13}C-CB) procured from Millipore-Sigma was used and mixed with varying ratios of nonisotopically enriched CB *via* simple mortar and pestle grinding or ball milling. Once mixed, FJH (Figure 1A, with experimental details in Figure S1 and Table S1) affords the ^{13}C-isotopically enriched tFG in seconds, affording gram-scale quantities (sample sizes ranging from 50 mg to 1 g). All characterization data here are shown after no further purification. Raman spectroscopy is regarded as a standard for graphene characterization due to the wealth of information a single spectrum can convey.[34] Peak location depends on both the wavelength of excitation as well as isotopic content since Raman spectroscopy is a vibrational technique and changes in nucleus mass impact the vibrational frequencies and modes. Traditionally, the most significant and well-known peaks are the D, G, and 2D occurring at ~1350, ~1600, and ~2690 cm^{-1}, respectively, when using a 532 nm excitation laser source and studying typical ^{12}C-graphene. However, higher resolution data can afford many other peaks that allow conclusions to be drawn regarding the spatial organization of individual graphene sheets in the bulk material.[35] The TS_1 and TS_2 (turbostratic 1 and 2,

https://doi.org/10.1021/acsnano.1c03197
ACS Nano 2021, 15, 10542−10552

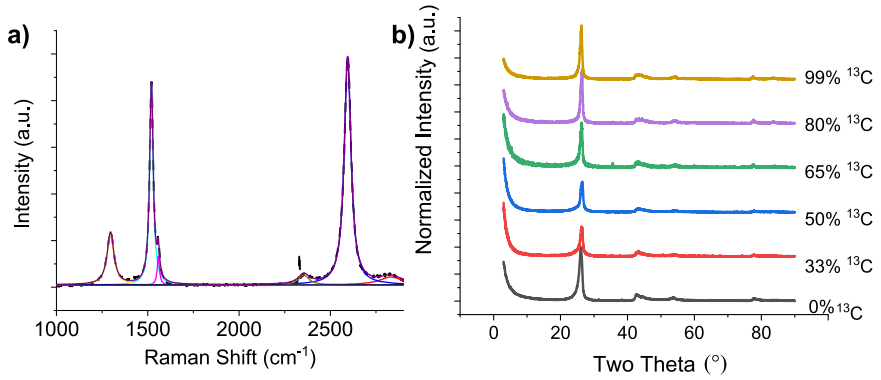

Figure 2. (a) Lorentzian fitting of a Raman spectrum of 99% ^{13}C tFG (spectrum: dotted black line; fitting curves: colored solid lines), displaying an R^2 value of 0.995. The small feature at ~2300 cm^{-1} results from atmospheric N_2. (b) Powder XRD characterization of the tFG samples with varying concentrations of ^{13}C.

respectively), present at 1875 and 2025 cm^{-1}, respectively, are indicative of the rotational disorder present in the stacking of individual graphene layers. Further, the M peak at 1750 cm^{-1} is observed in systems with ordered AB stacking and is expectedly absent here due to the turbostratic arrangement. Many reviews have been written on the Raman spectral analysis of graphene,[36−39] and the phonon modes of transitions are discussed below. Figure 1b shows the high quality of tFG produced, as demonstrated by the small D peak, large 2D/G ratio, and narrow 2D full width at half-maximum (fwhm) for all isotopic ratios produced. The fwhm of the 2D peaks at each isotopic ratio was determined using Lorentzian fitting and is shown in Table S2. A maximum in fwhm (42.9 cm^{-1}) is observed at an even 50−50 isotopic mixture; however a single Lorentzian still demonstrates a 0.998 *R*-squared value of fit. This increase in fwhm corresponds with the maximum configurational entropy of the system being achieved. As expected, a steady decrease in the Raman shift of all peaks is observed as the ^{13}C content is increased, in accordance with the harmonic approximation (specific values shown in Table S2). We have tabulated the peak position and fwhm of the TS1 and TS2 peaks observed as a function of ^{13}C content in Table S2b. Peak width again confirms that good isotopic mixing has occurred during the FJH process.

It is observed that the shift in peaks is consistent with the hypothesized $\frac{\sqrt{12}}{\sqrt{13}}$ relationship.[27] Moreover, the absence of two distinct pairs of D, 2D, and G peaks (one corresponding to ^{13}C graphene and the other to ^{12}C graphene) but rather the steady shift of the single D, 2D, and G peaks suggests that high degrees of sample homogeneity and mixing are achieved during FJH, with intermediate concentrations of ^{13}C resulting in slight broadening, possibly due to increases in configurational entropy of the lattice. This is consistent with the "mobile carbon" mechanism that has been proposed for FJH.[33] Figure 1c shows that all of the synthesized samples are turbostratic since the M peak at ~1750 cm^{-1}, which is indicative of AB stacking, is silent, and the TS_1 and TS_2 peaks, at ~1875 and 2025 cm^{-1}, respectively, are confirmations of the turbostratic orientation.[35] The position of the 2D and G bands can convey significant information about the mechanical state (strained or suspended) or electronic state (hole or heteroatom doping).[40] To our knowledge, no plot of this kind is reported for varying isotopic ratios of graphene, so such a plot (Figure S2a) may be of interest in further studies of isotopically enriched graphene materials. Further, the fwhm of the 2D and G peaks can convey important information about the configuration of graphene sheets, so such a plot is presented in Figure S2b, demonstrating a largely linear relationship between the fwhm of the G and 2D peaks with the exception of the 50% ^{13}C sample, where a significantly larger fwhm of the 2D peak is observed.[41] This again relates to the maximum in configurational entropy that is achieved at this isotopic ratio.

The turbostratic nature of the synthesized tFG can be further confirmed by the fitting of a single Lorentzian function to the 2D peak in a representative 99% ^{13}C-enriched tFG sample (Figure 2a). When multiple sheets are arranged in an AB stacked fashion, the 2D peak no longer exhibits a good fit by a single Lorentzian function, and the fwhm increases.[38] In the fitted spectrum, an fwhm of 34 cm^{-1} of the 2D peak is shown. This demonstrates how the electronically decoupled nature of tFG sheets can spectroscopically resemble monolayer graphene. The tFG was also characterized by powder X-ray diffraction (XRD), shown in Figure 2b. As expected, the interlayer spacing did not vary as a function of isotopic enrichment. This is due to the electronically identical nature and virtually indistinguishable atomic sizes, with attometer-scale differences for ^{13}C and ^{12}C. The diffraction angle of the (002) plane of all isotopic ratios is 26.28 ± 0.15°, corresponding to an interlayer spacing of 3.43 ± 0.02 Å, compared to 3.37 Å that is observed for AB-stacked graphite. This result, when combined with the broader and asymmetric nature of the (002) peak, is further evidence of the turbostratic arrangement of the FG.

Thermogravimetric analysis (TGA) of the tFG (Figure S3) shows the expected thermal stability of graphene, in excess of 660 °C under an air atmosphere. The TGA also confirms that the starting material has been well converted to tFG since no weight loss is observed well past the thermal stability of the starting ^{13}C−CB. The ^{13}C starting material (Figure S4) shows amorphous and graphitic character *via* Raman spectroscopy, as characterized by the intense D peak and broadening of the 2D peak. These characteristics are not observed in the enriched tFG, signifying that even partially graphitized feedstocks can be converted to tFG through FJH.

High degrees of elemental purity are essential to obtain meaningful conclusions from degradation, toxicity, and environmental impact, since false reports of toxicity or other erroneous conclusions may result from trace metal impurities such as Mn in GO.[42] XPS was carried out to determine the elemental purity of the tFG. Survey scans (Figure S5a) and detailed elemental content (Table S3) show high-purity

https://doi.org/10.1021/acsnano.1c03197
ACS Nano 2021, 15, 10542−10552

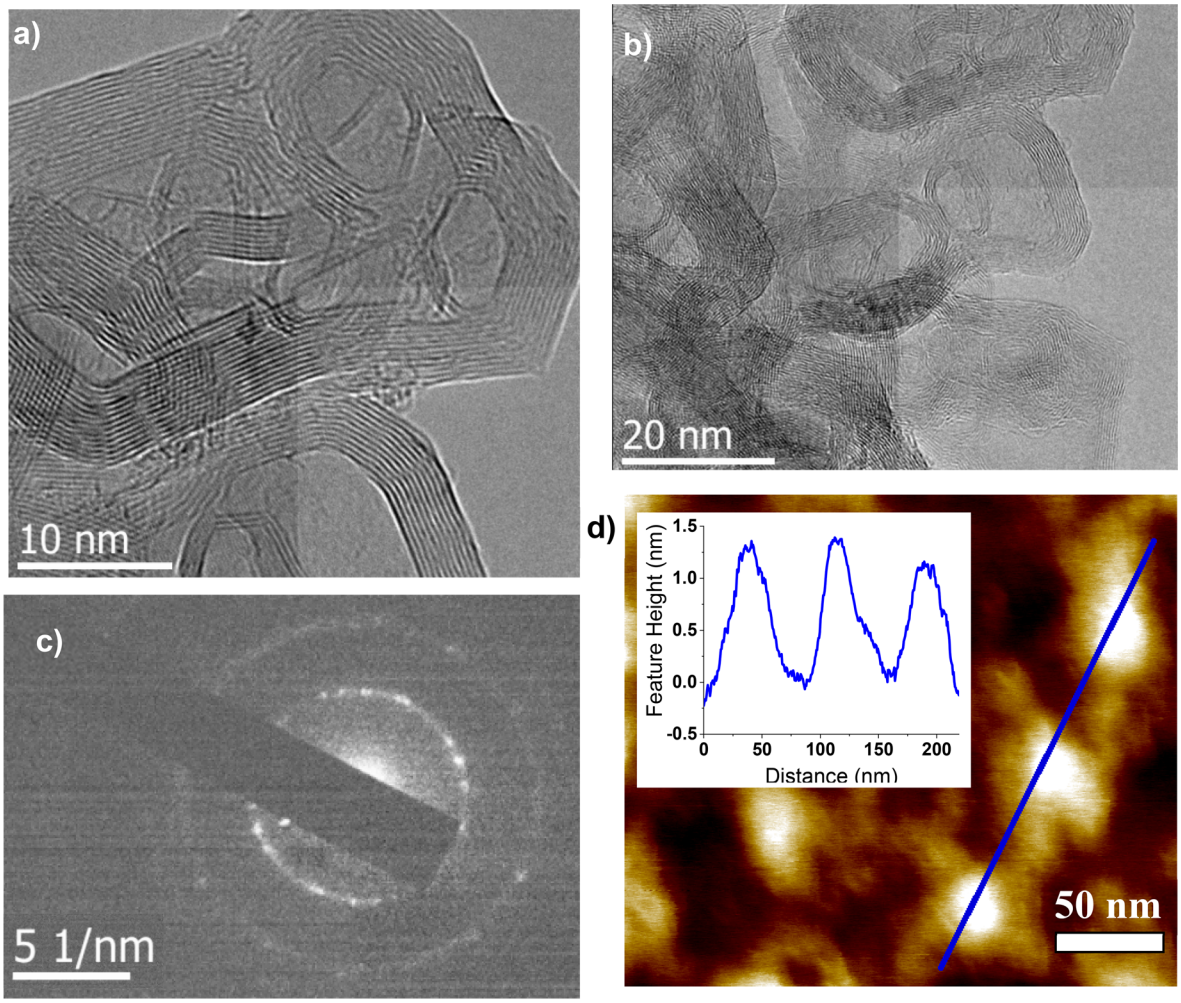

Figure 3. (a) Representative TEM image of 99% ^{13}C tFG sheets. (b) Representative TEM image of 33% ^{13}C-enriched tFG sheets. (c) SAED images of 99% ^{13}C-tFG. (d) AFM characterization of 99% ^{13}C-tFG sheets. Scale bar is 50 nm.

pristine graphene is formed through FJH, with only 0.53% oxygen content remaining. High-resolution XPS fitting (Figure S5b) of the C 1s peak shows that 98% of the peak area is attributed to C═C or C−C bonding, with a noticeable $\pi-\pi^*$ feature as well at 291.1 eV, confirming the homogeneous aromatic carbon bonding within the synthesized tFG.

Further, inductively coupled plasma mass spectrometry (ICP-MS) was carried out to determine the trace metal contamination present in 99% ^{13}C-tFG, as compared to the 99% ^{13}C amorphous carbon starting material and commercially available graphene (Tianyuan Empire Materials & Technologies, Shatin, Hong Kong). The isotopically enriched flash graphene was demonstrated to contain on average 59% less trace metals and up to 96% less cobalt than commercially available graphene (Figure S6). Interestingly, the produced tFG was also found to contain significantly less trace metals than the ^{13}C starting material, on average having 40% less metal. This confirms our hypothesis that non-carbon atoms are able to sublime out during the FJH process, since the temperature during FJH can surpass 3000 K, purifying the starting material during the graphene formation process.

The sheet size of the tFG is an important physical characteristic that might affect its solubility, environmental retention, and biological toxicity. The sheet size was observed through transmission electron microscopy (TEM) imaging (Figure 3), yielding sizes ranging from ∼20 to 40 nm. The TEM images show few-layer graphene (Figure 3a,b) that is turbostratically layered on top of each other (Figure 3c). Atomic force microscopy (AFM) imaging allows for accurate vertical and approximate horizontal size determination, and it agrees with TEM-determined sheet size. A histogram measuring the diameter of 80 different graphene sheet regions is shown in Figure S7. Notably, after simple sonication and casting on freshly cleaved mica, a sheet thicknesses of ∼1.3 nm can be observed. This is consistent with literature values for noncontact mode AFM of monolayer graphene, which can range from 0.4 to 1.6 nm in thickness depending on the peak force, tip, and substrate used.[43] The turbostratic nature results in much weaker electronic interactions and coupling between sheets, as shown by the increased interlayer spacing. This results in the tFG being far easier to exfoliate to single-sheet thickness, which is essential in the study of monolayer graphene, as opposed to few- and multilayer graphene or graphite. Furthermore, it has been shown that by varying the feedstock carbon source, FJH will produce a large range of sheet sizes, from ∼13 nm to ∼1 μm, as well as multiple different morphologies.[31,33,44,45]

Due to the decreased contribution of $\pi-\pi$ stacking interactions in tFG, the powder can be easily exfoliated using sonication, as opposed to requiring ball milling or chemical

https://doi.org/10.1021/acsnano.1c03197
ACS Nano 2021, 15, 10542−10552

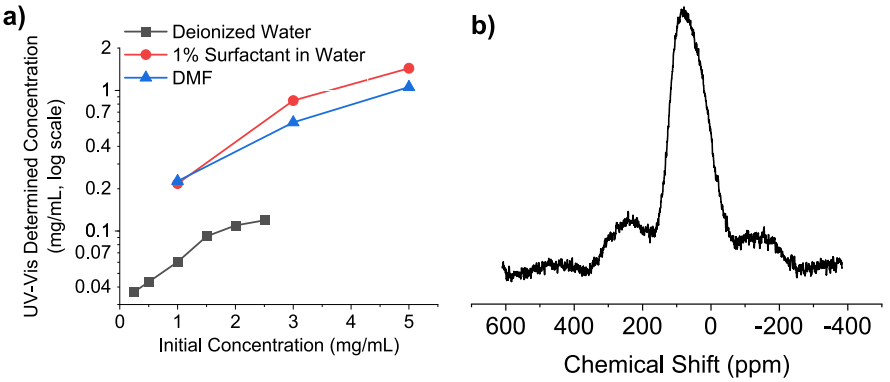

Figure 4. (a) UV−vis spectroscopy measured concentrations of 99% ^{13}C-enriched tFG dispersed in aqueous, surfactant-assisted, and organic solvents. (b) A 50.3 MHz, direct ^{13}C pulse, NMR spectrum of 50% ^{13}C-enriched tFG obtained with 10 kHz MAS with 90 s relaxation delay.

exfoliation. High dispersibility of the tFG is exemplified in Figure 4a. Concentrations lower than 0.1 mg/mL in deionized water are used in geologic and biologic studies and are readily achieved through sonication, followed by centrifugation to remove larger aggregates. This method yields solutions of high-quality isotopically enriched tFG, which was demonstrated through drop casting on a silicon wafer followed by Raman spectroscopic analysis (Figure S8). Analysis of the drop-cast area confirms that the dispersed compound is indeed graphene and showed good homogeneity over a large area, with a slight increase in D band intensity due to the sonication treatment. Surfactant-assisted aqueous systems and organic solvent show that dispersed concentrations of graphene in excess of 1.3 mg/mL can be attained.

Due to the promising solubility of tFG in aqueous and dimethylformamide (DMF) solutions or dispersions, liquid phase NMR was attempted. The stable colloidal dispersion of 80% ^{13}C-enriched graphene in D_2O with 0.05 wt % TSP-d_4[$(CH_3)_3$Si-CD_2CD_2-COONa] as a chemical shift reference yielded ^{13}C signals only for the salt. Less graphene could be dispersed in D_2O with 0.75 wt % TSP-d_4. Even without the salt, insufficient graphene could be dispersed to afford a detectable NMR signal. Similarly, a stable colloidal dispersion of 50% ^{13}C-enriched graphene in DMF-d_7 with 0.05 wt % TMS yielded ^{13}C signals only for the solvent and TMS; the S/N was high enough that even the CHD_2 quintet for each methyl group in DMF-hd_6 and the ^{29}Si satellites for ^{29}Si($^{13}CH_3$)-($^{12}CH_3$)$_3$ are evident. With either solvent, the probe tunes properly and the tube spins properly. Ring currents likely result in a severe broadening of the graphene ^{13}C signals, making them virtually spectroscopically silent. We are not aware of any literature solution state graphene spectra.

However, in the solid state, with the sheets stacked at random twist angles, a relatively simple Hahn echo, direct ^{13}C pulse, MAS NMR spectrum on 50% ^{13}C-enriched graphene could be obtained (Figure 4b). Lengthening the relaxation delay from 10 s to 30 s to 90 s resulted in a steady increase in signal intensity; the nuclei relax rather slowly (Figure S9). The weaker broad signals on either side of the main signal are spinning sidebands, as these weaker broad signals are absent if the sample is not spinning; the signal is also significantly broader without spinning (Figure S10).

Averaging of the chemical shift anisotropy by spinning at 10 kHz is clearly significantly less than would be achieved with an ordinary organic solid. Spinning much faster than 10 kHz would be desirable in order to displace the spinning sidebands further from the centerband and possibly further narrow the centerband. However, much faster spinning was not possible, since the 4 mm diameter rotor has a nominal maximum spinning speed of 15 kHz, and the drive air pressure that would spin an ordinary solid at 12 kHz would spin the graphene sample at only 10 kHz. Still, it is worth keeping in perspective the severe challenges that are encountered just in sample spinning and probe tuning with a rotor containing graphite, where the sheets in the powder are layered in an A−B Bernal-stacked manner.[46−48]

The main signal in the MAS spectrum of the turbostratic 50% ^{13}C-enriched graphene has a maximum at ∼80 ppm, which is clearly upfield of the region for aromatic carbon signals in ordinary polycyclic aromatic compounds; upfield of the chemical shift of a sample of very highly reduced graphite oxide,[47] and similar to the chemical shift of bulk graphitic materials.[49−52] These observations are consistent with calculations indicating increasing shielding of the more interior nuclei in graphene sheets as the sheet size increases.[53,54]

A ^{1}H−^{13}C cross-polarization experiment with a 1 ms contact time yielded only noise. From a single experiment, it is not clear if the absence of any ^{13}C signal results from very few carbons on the periphery (where protons can be bound) relative to the number of interior carbons, from a very short ^{1}H spin−lattice relaxation time in the rotating frame, from a very long ^{1}H spin−lattice relaxation time in the laboratory frame, or from some combination of factors. However, the inability to detect a ^{13}C signal in the CP experiment, the broad, rather shielded signal in the direct ^{13}C pulse experiment, and the ability to spin the sample at only 10 kHz with a drive air pressure that would spin an ordinary solid at 12 kHz are all very similar to the observations with a sample of very highly reduced graphite oxide.[47]

In light of the success with the relatively simple direct ^{13}C pulse MAS experiment, an obvious follow-up experiment would be to study ^{13}C-enriched graphene with much faster spinning in a significantly smaller rotor at a modest field strength so that the spinning sidebands could be displaced much further from the centerband. Of course, the significantly reduced sample size would correspondingly reduce S/N per unit time. However, this could, in principle, be overcome by using signal enhancement techniques combining Carr−Purcell−Meiboom−Gill (CPMG) pulse trains that use π pulses to repeatedly refocus and observe signals as long as transverse magnetization persists with magic angle spinning to refocus anisotropic interactions.[55] The S/N enhancement in a

https://doi.org/10.1021/acsnano.1c03197
ACS Nano 2021, 15, 10542−10552

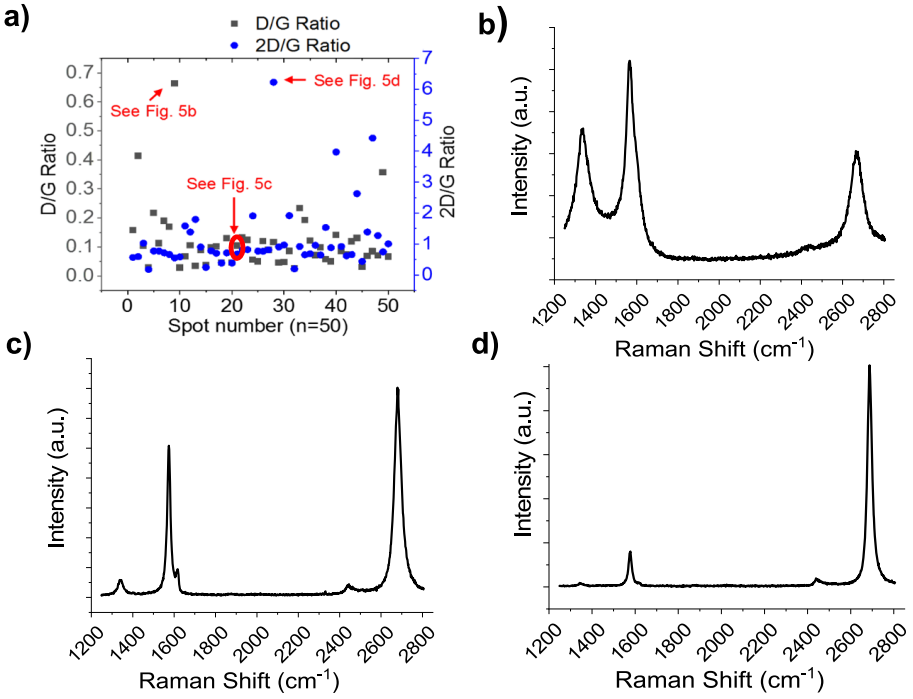

Figure 5. (a) Scatter plot showing the 2D:G ratio and D:G ratio of Raman scattering intensities from randomly selected areas from a 3.2 g, 5% ^{13}C-enriched tFG sample. (b) Spectrum showing the highest D:G ratio observed. (c) Representative spectrum of the bulk synthesized tFG. (d) Spectrum showing the highest 2D:G ratio observed in the tFG in the 50 spectra.

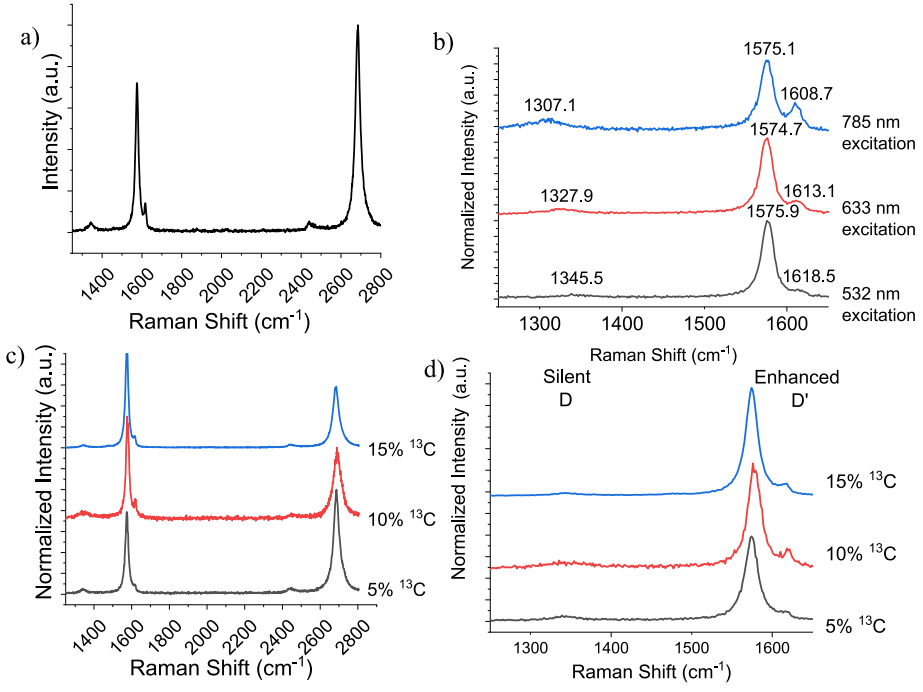

Figure 6. (a) D′ enhancement in 10% ^{13}C-enriched tFG at 532 nm excitation. (b) Excitation wavelength dependence of the D′ peak in 10% ^{13}C-enriched tFG with peaks labeled from Lorentzian fits. (c) Other representative spectra showing bulk D′ enhancement in 5−15% ^{13}C-enriched tFG with 532 nm excitation. (d) Magnified spectra showing bulk D′ enhancement in 5−15% ^{13}C-enriched tFG with 532 nm excitation.

^{13}C CPMG-MAS spectrum of a few milligrams of graphene nanosheets relative to a standard ^{13}C MAS spectrum is obvious; indeed, with a sufficient number of spikelets, the line shape is readily apparent.[55]

To demonstrate that large-scale studies and applications of ^{13}C-enriched graphene such as soil and aquafer tracing are achievable, we synthesized a large batch of graphene that was only slightly enriched to minimize the cost. Using the FJH method, a 3.2 g batch of 5% ^{13}C-graphene was synthesized from 5% ^{13}C-CB and 95% ^{12}C-CB in <1 h. Even in such large batches, the tFG is very high quality and homogeneous, as shown by 50 randomly selected Raman spectra (Figure 5). The

https://doi.org/10.1021/acsnano.1c03197
ACS Nano 2021, 15, 10542−10552

scatterplot shows the distribution of 2D/G intensity and D/G intensity. Three spots, labeled in panel a, have their Raman spectra shown in panels b–d. Excellent quality graphene has a high 2D/G ratio and low D/G ratio. Only 6% of samples have significant D band character (average D/G ratio 0.12), and the average 2D/G ratio is 1.13. The turbostratic arrangement of the 3.2 g batch is also confirmed through the spectroscopic presence of TS_1 and TS_2 peaks, as well as the absence of the M peak (Figure S11).

Interestingly, throughout the synthesis and characterization of tFG samples with low values of ^{13}C-enrichment, a pronounced enhancement of what has been established to be the D′ peak (~1600 cm^{-1} for pure ^{12}C-tFG using a 532 nm excitation source) is observed. The D′ enhancement is most intense at 10% ^{13}C-enrichment (Figure 6, also visible in Figure 5c). The identity of the D′ band, as opposed to the R′ band that occurs at the same Raman shift and indicates very low angle stacking in turbostratic graphene, was confirmed by varying the excitation source wavelength.[56] Because the D′ band is dispersive and the R′ band is not, a clear shift in peak location is evident once Lorentzian fitting is done. The amount of dispersion is consistent with the few other literature reports that discuss the D′ band, confirming the peak's identity (Figure 6b–d).[57] The dispersive nature of the D′ band can also be compared to the nondispersive nature of the G band, which, as expected, shows no significant shift when the excitation wavelength is varied. The D peak shows significant dispersion, in agreement with literature sources.[37] The D′ peak is relatively unstudied but can be pronounced for zigzag edges present in small sheets (<5 nm size).[58] This is because the D peak is symmetry forbidden for zigzag edges, and there is no wavevector that can bring the electron from the K to the K′ point. However, as discussed earlier, TEM images show larger sheets, and this effect is not observed at other ^{13}C-doping concentrations, so it might be that the D′ enhancement is not caused by the edge contributions of extremely small sheets. The reason that the D′ is active, but the D is not for zigzag edges, is that there is no wavevector that can bring the electron from the K to the K′ point for the zigzag edge that conserves momentum (thus, the D mode is symmetry forbidden for the zigzag edge). Substitution in mass breaks the symmetry of the lattice, which decreases K to K′ scattering due to a slight difference in phonon energy. However, K to K intravalley elastic scattering is still allowed, and it is enhanced by both increased "defect" concentration and increased lifetime of the phonon due to disfavored K to K′ scattering. Therefore, the D′ band grows. Substituting a single atom in a graphene lattice generates an edge of 12 atoms that surrounds the single substituted atom. The zigzag portions are directly connected to the ^{13}C, whereas the armchair edges are indirectly connected. Three zigzag paths can be drawn through the ^{13}C atom, whereas 6 + 6 armchair configurations can be drawn. So, this decreases the D peak while simultaneously enhancing the D′ peak.[39]

The mechanism for the D′ enhancement might arise from the frequency-dependent nature of the D′ peak. Elastic scattering at the K point is enhanced due to the isotopic substitution that perturbs local symmetry. Low isotopic enrichment (5–15% ^{13}C) results in a favorable enhancement of the D′ phonon mode by varying the vibrational frequency of the graphene lattice. The vibrational frequency changes as a function of isotopic ratio, and at these low isotopic ratios the D′ phonon reaches a more favorable vibrational frequency for D′ resonance. This is supported by the dispersive nature of the D′ peak, as well as the migration in Raman shift as the isotopic content is varied. The dispersive nature results from the excitation photon exciting to higher or lower energy levels as it is varied, while the D′ signal enhancement comes from the match in vibrational frequency of the lattice to the vibrational frequency of the intravalley scattering. This matching of resonances results in a higher likelihood for Raman scattering (photon re-emission) as opposed to nonemissive pathways that occur following intravalley excitation. Further, the substitution might break the symmetry between the K and the K′ points, which suppresses the intervalley "defect" scattering event (elastic). Thus, the D peak is suppressed. As shown in Figure 7, the D′ peak results from a double-resonance mode that also

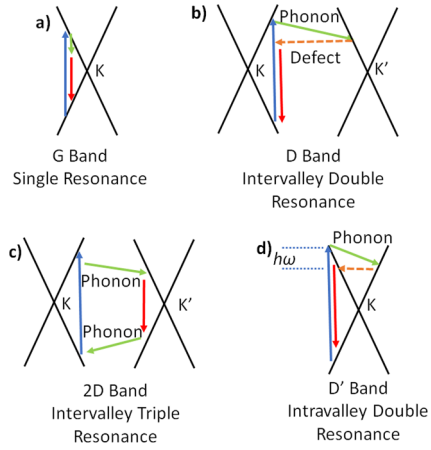

Figure 7. Dirac cone schematics highlighting the observed Raman-active processes and phonon dispersions that give rise to the (a) G band; (b) D band; (c) 2D band; and (d) D′ band.

requires the presence of a defect in the graphene lattice to complete the intravalley transition.[36] Since a defect is required for the D′ resonance mode to be active, and the D peak is an intervalley mode that also requires a defect, it is exceedingly rare that the D′ peak is more intense than the D peak.[37] The D′ peak is only larger than the D peak when in-plane longitudinal optical (iLO) phonons are favored, showing a peculiar predilection for intravalley scattering, as opposed to the more active intervalley scattering mode.[59] iLO phonons are an in-plane bending mode, which was recently reported to be indicative of strained graphene, with reported pseudomagnetic field effects.[60] Intravalley scatter also impacts the charge and thermal transport of the FG, through disruption of the electron–hole recombination rate.[61] As shown in Figure 7d, the D′ scattering process depends completely on the vibrational energies of both the imparted phonon and defect. Through Hooke's law we understand how the vibrational frequency of the graphene system depends closely on the isotopic ratio, and the energy is inversely proportional to the increase in mass as ^{13}C replaces ^{12}C in the sheets. This effect results in all peaks shifting in the Raman spectra, but it also appears at ~10% ^{13}C enrichment. The vibrational frequency favors intravalley double resonance, therefore resulting in the observed D′ enhancement. This selective and controllable D′ enhancement is important for characterization of the phonon properties and pseudomagnetic field effects that are certainly of interest in solid state physics. Selectivity between intravalley and intervalley scattering is an emerging approach in bandgap

https://doi.org/10.1021/acsnano.1c03197
ACS Nano 2021, 15, 10542–10552

engineering in graphene, which might lead to advanced transistors or semiconducting materials.[61]

Inspired by the high degree of homogeneity of carbon isotopes composing the tFG, it was supposed that many aromatic $^{12}C{=}^{13}C$ bonds exist within the material. Due to the nonsymmetric nature of these bonds, it was hypothesized that they would be IR visible due to the active vibrational moment that is now present, as the structurally similar boron nitride is IR-active due to nonsymmetric bonds. The clear presence of an aromatic $^{12}C{=}^{13}C$ bond stretching is shown in Figure 8,

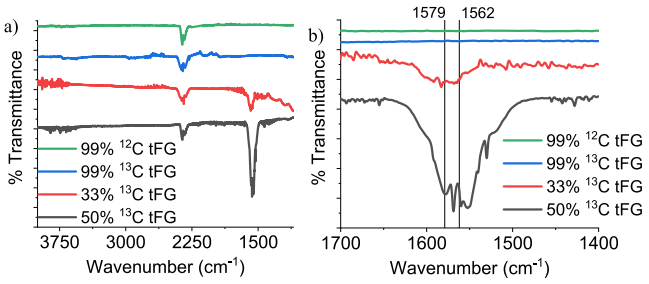

Figure 8. (a) FT-IR of graphene, with varying concentrations of ^{13}C enrichment. (b) Enlarged spectra showing the aromatic $^{12}C{=}^{13}C$ stretch in graphene.

centered at 1562 cm^{-1} in the tFG sample that is 50:50 ^{12}C:^{13}C, which appears due to the development of a transient local dipole. This peak is shifted slightly in the sample that is 67:33 ^{12}C:^{13}C, occurring at 1579 cm^{-1}, as well as being less intense due to the lower occurrence of the nonsymmetric aromatic $^{12}C{=}^{13}C$ bond. A shift in the absorbance band is expected as isotopic content varies; however, it is normally a larger shift such as ~70 cm^{-1} in CO_2.[62] Although it is not a direct comparison between $^{13/12}C{=}O$ bonds to $^{12/13}C{-}C$ bonds, it illustrates the shift in absorption wavenumber as a function of isotopic ratio is much more dramatic in discrete small molecule systems. In the tFG system, the large size of the sheets, which can be regarded as a single molecule, results in the broadening and much less significant shift due to the bulk nature and less nonideally defined system when compared to traditional small molecules. This is in agreement with a recent study of isotopically enriched calcite, which showed a small shift of ~20 cm^{-1} as ^{13}C-content was increased from 0% to 99%.[63] The smaller shift in crystals is due to the nonideal crystal system resulting in the entire mass of all atoms that are moving being included in the mass matrix, rather than a simple unit cell or single gas molecule. Likewise, the force matrix contains all the interactions from all those atoms. Therefore, the difference in observed frequency for the system is much less than if it were just two masses on a spring. To our knowledge, no IR spectrum of graphene has been reported, even in the few that studied isotopically enriched graphenes. Attenuated total reflectance (ATR) was used to collect the data, and the ambient CO_2 stretches are also present. Due to the pristine nature of the graphene, no oxygen-related functional groups are observed, and due to the size of the sheets, no edge C−H functionalities are shown in the spectra.

CONCLUSION

In conclusion, we present a facile route to bulk synthesis of ^{13}C-enriched tFG, capable of achieving any desired isotopic ratio. The characterization data show ^{13}C NMR, Raman-active D′ peak enhancement, and an FT-IR spectrum of graphene. This bulk material might provide a source for the much needed environmental and biological fate studies of graphene.

EXPERIMENTAL SECTION

Chemicals and Materials. Cabot Black Pearls 2000 ^{12}C amorphous carbon black was used as received from Cabot Corporation. ^{13}C amorphous carbon (99 atom %) was used as received from Millipore-Sigma. Pluronic-F127, a nonionic surfactant, was obtained from Millipore-Sigma. DMF, HPLC grade >99.9%, was used as received from Millipore-Sigma, and DI water was used for surfactant-assisted dispersion studies. Ethanol, 200 proof, was used as received from Millipore-Sigma. Commercial graphene samples used for comparison were obtained from Tianyuan Empire Materials & Technologies, Shatin, Hong Kong, and used without further purification.

Synthesis of tFG. For the synthesis of tFG, a specially designed FJH station was built for the conversion of carbon feedstock to tFG as previously reported.[33] Further details, including a specific circuit schematic, photographs, safety considerations, and design details, are shown in Figure S1. A varying amount of capacitance was used depending on the batch size, which ranged from 50 mg to 1 g. Carbon sources were ground with a mortar and pestle or ball milled before being compressed in a quartz tube between graphite plugs to enclose the sample during heating. Further conversion details are given in Table S1. The sample, encased in a quartz tube, was loaded into a vacuum desiccator, and the FJH apparatus was used to apply the electronic discharge pulse(s). After the FJH, the tFG was removed from the quartz tube and ground with a mortar and pestle. Yields of 85−90% were typically observed. tFG was used without any further purification.

Dispersions of tFG in Various Solvent Systems. Varying amounts of ground tFG powder were weighed into centrifuge tubes, and solvent was added to yield the initial loading concentration (~1 mg tFG powder/mL of solvent). The centrifuge tubes were then cup-horn-sonicated for 30 min and centrifuged at 550 relative centrifugal force for 15 min to remove larger aggregates. The dispersions were then used for UV−vis, AFM, and TEM characterization.

Characterization and Measurements. *Raman Spectroscopy.* All Raman spectra were collected from samples of tFG after grinding with a mortar and pestle to ensure sample homogeneity. A Renishaw inVia Raman microscope outfitted with a 5 mW 532 nm laser, a 5 mW 633 nm laser, and a 5 mW 785 nm laser was used. A 50× objective lens was used to collect all Raman spectra. For dispersion studies, a pinhole was used to ensure the same spot was observed with varying excitation wavelength, and each wavelength was calibrated using the internal silicon reference before spectra collection. Analysis of Raman spectra, including peak intensity ratios, uses the height of the peak. All peak positions were determined through baseline correction, Lorentzian fitting, and peak deconvolution.

X-ray Diffraction. All powder XRD spectra were collected on samples ground by a mortar and pestle. To collect spectra, a Rigaku D/Max Ultima II Powder XRD 6S was used. A scan width of 0.05°/step and scan rate of 0.5°/min was used from 3° to 90°. Zero background sample holders were used.

Thermogravimetric Analysis. TGA thermograms were collected using a TA Instruments Q-600 simultaneous TGA/DSC using alumina pans, with a heating rate of 10 °C/min up to 780 °C. An air atmosphere, at a flow rate of 80 mL/min, was used to purge the sample chamber.

Fourier Transform Infrared Microscopy. All FT-IR spectra were collected on a Nicolet iN10 FT-IR infrared microscope using an ATR attachment. Background spectra were collected, and 128 spectra were averaged to yield adequate signal-to-noise.

UV−Vis Absorption Spectroscopy. Using the tFG/solvent dispersions prepared as detailed above, the supernatant was decanted after centrifugation and diluted 200× with the parent solvent since the graphene concentration makes the absorbance very high. The absorbance at 660 nm was measured and the graphene concentration

https://doi.org/10.1021/acsnano.1c03197
ACS Nano 2021, 15, 10542−10552

was determined using Beer's law with an extinction coefficient of 6600 l/g·m. Quartz cuvettes, with simultaneous baseline correction, were used.

X-ray Photoelectron Spectroscopy. XPS data were collected using a PHI Quantera SXM scanning X-ray microprobe using a base pressure of 5×10^{-9} Torr. Survey spectra were recorded using 0.5 eV step sizes with a pass energy of 140 eV. Elemental spectra were recorded using 0.1 eV step sizes with a pass energy of 26 eV. All of the XPS spectra were corrected using the C 1s peaks (284.6 eV) as reference.

Atomic Force Microscopy. Tapping-mode was used with a Park NX20 AFM on samples of heavily diluted samples of tFG dispersed in ethanol that were drop cast onto freshly cleaved mica.

Nuclear Magnetic Resonance. In contrast to the eddy currents in and resulting high electrical conductivity of graphite[52,64] that cause tremendous problems in spinning a rotor and tuning the probe,[46−48] these effects were much smaller with the turbostratic 50% ^{13}C-enriched graphene. This improvement could be attributed to the stacking of the sheets at random twist angles (unlike the ordered AB arrangement of sheets in hexagonal graphite). The spinning speed was not quite as stable as with an ordinary solid, but the spinning speed fluctuations were small (~±5 Hz). Compared to a glycine standard, the spinning graphene sample had relatively little effect on tuning the ^{13}C channel in the probe and almost no effect on tuning the ^{1}H channel, but the ^{13}C matching and ^{1}H matching required significant adjustments. Spectrometer and data acquisition details have been reported previously.[65]

Transmission Electron Microscopy. TEM and selected area electron diffraction (SAED) images were obtained on a JEOL 2100 field emission transmission electron microscope at an acceleration voltage of 200 kV. Samples were prepared by drop casting a dilute tFG/ethanol solution onto lacey carbon grids.

Inductively Coupled Plasma Mass Spectrometry. ICP-MS was obtained using an Agilent 8800 ICP-QQQ-MS. Samples were prepared by digesting 1 mg/mL of material in 1 M nitric acid (Millipore, Ultrapure grade) at 50 °C for 24 h, filtered over a PTFE membrane with a 0.3 μm pore size, and then diluted to volume with 2% nitric acid. Elemental calibration curves were carried out using standards (PerkinElmer) at four different concentrations over 4 orders of magnitude.

ASSOCIATED CONTENT

Supporting Information

The Supporting Information is available free of charge at https://pubs.acs.org/doi/10.1021/acsnano.1c03197.

Circuit diagram, photo of apparatus, and additional graphs and spectra (PDF)

AUTHOR INFORMATION

Corresponding Author

James M. Tour − *Department of Chemistry, Smalley-Curl Institute, NanoCarbon Center and Welch Institute for Advanced Materials, and Department of Materials Science and NanoEngineering, Rice University, Houston, Texas 77005, United States;* orcid.org/0000-0002-8479-9328; Email: tour@rice.edu

Authors

Kevin M. Wyss − *Department of Chemistry, Rice University, Houston, Texas 77005, United States*

Zhe Wang − *Department of Chemistry, Rice University, Houston, Texas 77005, United States*

Lawrence B. Alemany − *Department of Chemistry and Shared Equipment Authority, Rice University, Houston, Texas 77005, United States;* orcid.org/0000-0001-7451-1020

Carter Kittrell − *Department of Chemistry, Rice University, Houston, Texas 77005, United States;* orcid.org/0000-0002-8449-4292

Complete contact information is available at: https://pubs.acs.org/10.1021/acsnano.1c03197

Notes

The authors declare the following competing financial interest(s): Universal Matter Inc. has licensed from Rice University the FJH approach to graphene. J.M.T. is a stockholder in Universal Matter, but not an employee, officer, or director. Potential conflicts of interest are mitigated through regular disclosures to and compliance with Rice University's Office of Sponsored Programs and Research Compliance.

ACKNOWLEDGMENTS

K.M.W. acknowledges the NSF GRFP for generous funding of the research. The authors also acknowledge the University of Houston ICP Analytical Laboratory and Agilent Facility Center for use of their ICP-QQQ-MS instrument. The Air Force Office of Scientific Research (FA9550-19-1-0296) and the DOE-NETL (DE-FE0031794) funded this work. Dr. Bo Chen assisted with XPS analysis.

REFERENCES

(1) Ye, R.; Tour, J. M. Graphene at Fifteen. *ACS Nano* **2019**, *13*, 10872−10878.

(2) Allen, M. J.; Tung, V. C.; Kaner, R. B. Honeycomb Carbon: A Review of Graphene. *Chem. Rev.* **2010**, *110*, 132−145.

(3) Balandin, A. A.; Ghosh, S.; Bao, W.; Calizo, I.; Teweldebrhan, D.; Miao, F.; Lau, C. N. Superior Thermal Conductivity of Single-Layer Graphene. *Nano Lett.* **2008**, *8*, 902−907.

(4) Lee, C.; Wei, X.; Kysar, J. W.; Hone, J. Measurement of the Elastic Properties and Intrinsic Strength of Monolayer Graphene. *Science* **2008**, *321*, 385−388.

(5) Papageorgiou, D. G.; Kinloch, I. A.; Young, R. J. Mechanical Properties of Graphene and Graphene-Based Nanocomposites. *Prog. Mater. Sci.* **2017**, *90*, 75−127.

(6) Fang, B.; Chang, D.; Xu, Z.; Gao, C. A Review on Graphene Fibers: Expectations, Advances, and Prospects. *Adv. Mater.* **2020**, *32*, 1902664.

(7) Galashev, A. E.; Rakhmanova, O. R. Mechanical and Thermal Stability of Graphene and Graphene-Based Materials. *Phys.-Usp.* **2014**, *57*, 970.

(8) Castro Neto, A. H.; Guinea, F.; Peres, N. M. R.; Novoselov, K. S.; Geim, A. K. The Electronic Properties of Graphene. *Rev. Mod. Phys.* **2009**, *81*, 109−162.

(9) Rozhkov, A. V.; Sboychakov, A. O.; Rakhmanov, A. L.; Nori, F. Electronic Properties of Graphene-Based Bilayer Systems. *Phys. Rep.* **2016**, *648*, 1−104.

(10) Naumis, G. G.; Barraza-Lopez, S.; Oliva-Leyva, M.; Terrones, H. Electronic and Optical Properties of Strained Graphene and Other Strained 2D Materials: A Review. *Rep. Prog. Phys.* **2017**, *80*, 096501.

(11) Cao, Y.; Fatemi, V.; Fang, S.; Watanabe, K.; Taniguchi, T.; Kaxiras, E.; Jarillo-Herrero, P. Unconventional Superconductivity in Magic-Angle Graphene Superlattices. *Nature* **2018**, *556*, 43−50.

(12) Kumar, A.; Sharma, K.; Dixit, A. R. A Review of the Mechanical and Thermal Properties of Graphene and Its Hybrid Polymer Nanocomposites for Structural Applications. *J. Mater. Sci.* **2019**, *54*, 5992−6026.

(13) Nieto, A.; Bisht, A.; Lahiri, D.; Zhang, C.; Agarwal, A. Graphene Reinforced Metal and Ceramic Matrix Composites: A Review. *Int. Mater. Rev.* **2017**, *62*, 241−302.

(14) Mohan, V. B.; Lau, K.; Hui, D.; Bhattacharyya, D. Graphene-Based Materials and Their Composites: A Review on Production,

Applications and Product Limitations. *Composites, Part B* **2018**, *142*, 200−220.
(15) Güler, Ö.; Bağcı, N. A Short Review on Mechanical Properties of Graphene Reinforced Metal Matrix Composites. *J. Mater. Res. Technol.* **2020**, *9*, 6808−6833.
(16) Zhang, Q.; Wu, Z.; Li, N.; Pu, Y.; Wang, B.; Zhang, T.; Tao, J. Advanced Review of Graphene-Based Nanomaterials in Drug Delivery Systems: Synthesis, Modification, Toxicity and Application. *Mater. Sci. Eng., C* **2017**, *77*, 1363−1375.
(17) Lavagna, L.; Meligrana, G.; Gerbaldi, C.; Tagliaferro, A.; Bartoli, M. Graphene and Lithium-Based Battery Electrodes: A Review of Recent Literature. *Energies* **2020**, *13*, 4867.
(18) Yang, Z.; Tian, J.; Yin, Z.; Cui, C.; Qian, W.; Wei, F. Carbon Nanotube- and Graphene-Based Nanomaterials and Applications in High-Voltage Supercapacitor: A Review. *Carbon* **2019**, *141*, 467−480.
(19) Han, T.-H.; Kim, H.; Kwon, S.-J.; Lee, T.-W. Graphene-Based Flexible Electronic Devices. *Mater. Sci. Eng., R* **2017**, *118*, 1−43.
(20) Li, M.; Chen, T.; Gooding, J. J.; Liu, J. Review of Carbon and Graphene Quantum Dots for Sensing. *ACS Sens.* **2019**, *4*, 1732−1748.
(21) Geim, A. K.; Novoselov, K. S. The Rise of Graphene. *Nat. Mater.* **2007**, *6*, 183−191.
(22) Martín, C.; Kostarelos, K.; Prato, M.; Bianco, A. Biocompatibility and Biodegradability of 2D Materials: Graphene and Beyond. *Chem. Commun.* **2019**, *55*, 5540−5546.
(23) Chen, M.; Qin, X.; Zeng, G. Biodegradation of Carbon Nanotubes, Graphene, and Their Derivatives. *Trends Biotechnol.* **2017**, *35*, 836−846.
(24) Zhao, J.; Wang, Z.; White, J. C.; Xing, B. Graphene in the Aquatic Environment: Adsorption, Dispersion, Toxicity and Transformation. *Environ. Sci. Technol.* **2014**, *48*, 9995−10009.
(25) Bai, H.; Jiang, W.; Kotchey, G. P.; Saidi, W. A.; Bythell, B. J.; Jarvis, J. M.; Marshall, A. G.; Robinson, R. A. S.; Star, A. Insight into the Mechanism of Graphene Oxide Degradation *via* the Photo-Fenton Reaction. *J. Phys. Chem. C* **2014**, *118*, 10519−10529.
(26) Yuan, J.; Gao, H.; Ching, C. B. Comparative Protein Profile of Human Hepatoma HepG2 Cells Treated with Graphene and Single-Walled Carbon Nanotubes: An ITRAQ-Coupled 2D LC-MS/MS Proteome Analysis. *Toxicol. Lett.* **2011**, *207*, 213−221.
(27) Chen, L.; Wang, C.; Li, H.; Qu, X.; Yang, S.-T.; Chang, X.-L. Bioaccumulation and Toxicity of ^{13}C-Skeleton Labeled Graphene Oxide in Wheat. *Environ. Sci. Technol.* **2017**, *51*, 10146−10153.
(28) Kauling, A. P.; Seefeldt, A. T.; Pisoni, D. P.; Pradeep, R. C.; Bentini, R.; Oliveira, R. V. B.; Novoselov, K. S.; Neto, A. H. C. The Worldwide Graphene Flake Production. *Adv. Mater.* **2018**, *30*, 1803784.
(29) Li, Y.; Liu, Y.; Fu, Y.; Wei, T.; Le Guyader, L.; Gao, G.; Liu, R.-S.; Chang, Y.-Z.; Chen, C. The Triggering of Apoptosis in Macrophages by Pristine Graphene through the MAPK and TGF-Beta Signaling Pathways. *Biomaterials* **2012**, *33*, 402−411.
(30) Liu, S.; Zeng, T. H.; Hofmann, M.; Burcombe, E.; Wei, J.; Jiang, R.; Kong, J.; Chen, Y. Antibacterial Activity of Graphite, Graphite Oxide, Graphene Oxide, and Reduced Graphene Oxide: Membrane and Oxidative Stress. *ACS Nano* **2011**, *5*, 6971−6980.
(31) Wyss, K. M.; Beckham, J. L.; Chen, W.; Luong, D. X.; Hundi, P.; Raghuraman, S.; Shahsavari, R.; Tour, J. M. Converting Plastic Waste Pyrolysis Ash into Flash Graphene. *Carbon* **2021**, *174*, 430−438.
(32) Tian, L.; Wang, X.; Cao, L.; Meziani, M. J.; Kong, C. Y.; Lu, F.; Sun, Y. P. Preparation of Bulk ^{13}C-Enriched Graphene Materials. *J. Nanomater.* **2010**, *2010*, 742167.
(33) Luong, D. X.; Bets, K. V.; Algozeeb, W. A.; Stanford, M. G.; Kittrell, C.; Chen, W.; Salvatierra, R. V.; Ren, M.; McHugh, E. A.; Advincula, P. A.; Wang, Z.; Bhatt, M.; Guo, H.; Mancevski, V.; Shahsavari, R.; Yakobson, B. I.; Tour, J. M. Gram-Scale Bottom-Up Flash Graphene Synthesis. *Nature* **2020**, *577*, 647−651.
(34) Ferrari, A. C.; Basko, D. M. Raman Spectroscopy as a Versatile Tool for Studying the Properties of Graphene. *Nat. Nanotechnol.* **2013**, *8*, 235−246.
(35) Garlow, J. A.; Barrett, L. K.; Wu, L.; Kisslinger, K.; Zhu, Y.; Pulecio, J. F. Large-Area Growth of Turbostratic Graphene on Ni(111) *via* Physical Vapor Deposition. *Sci. Rep.* **2016**, *6*, 19804.
(36) Wu, J.-B.; Lin, M.-L.; Cong, X.; Liu, H.-N.; Tan, P.-H. Raman Spectroscopy of Graphene-Based Materials and Its Applications in Related Devices. *Chem. Soc. Rev.* **2018**, *47*, 1822−1873.
(37) Merlen, A.; Buijnsters, J. G.; Pardanaud, C. A Guide to and Review of the Use of Multiwavelength Raman Spectroscopy for Characterizing Defective Aromatic Carbon Solids: From Graphene to Amorphous Carbons. *Coatings* **2017**, *7*, 153.
(38) Malard, L. M.; Pimenta, M. A.; Dresselhaus, G.; Dresselhaus, M. S. Raman Spectroscopy in Graphene. *Phys. Rep.* **2009**, *473*, 51−87.
(39) Lenski, D. R.; Fuhrer, M. S. Raman and Optical Characterization of Multilayer Turbostratic Graphene Grown *via* Chemical Vapor Deposition. *J. Appl. Phys.* **2011**, *110*, 013720.
(40) Ni, Z.; Wang, Y.; Yu, T.; You, Y.; Shen, Z. Reduction of Fermi Velocity in Folded Graphene Observed by Resonance Raman Spectroscopy. *Phys. Rev. B: Condens. Matter Mater. Phys.* **2008**, *77*, 235403.
(41) Pardanaud, C.; Merlen, A.; Gratzer, K.; Chuzel, O.; Nikolaievskyi, D.; Patrone, L.; Clair, S.; Ramirez-Jimenez, R.; de Andrés, A.; Roubin, P.; Parrain, J.-L. Forming Weakly Interacting Multilayers of Graphene Using Atomic Force Microscope Tip Scanning and Evidence of Competition between Inner and Outer Raman Scattering Processes Piloted by Structural Defects. *J. Phys. Chem. Lett.* **2019**, *10*, 3571−3579.
(42) Ye, R.; Dong, J.; Wang, L.; Mendoza-Cruz, R.; Li, Y.; An, P.-F.; Yacamán, M. J.; Yakobson, B. I.; Chen, D.; Tour, J. M. Manganese Deception on Graphene and Implications in Catalysis. *Carbon* **2018**, *132*, 623−631.
(43) Shearer, C. J.; Slattery, A. D.; Stapleton, A. J.; Shapter, J. G.; Gibson, C. T. Accurate Thickness Measurement of Graphene. *Nanotechnology* **2016**, *27*, 125704.
(44) Stanford, M. G.; Bets, K. V.; Luong, D. X.; Advincula, P. A.; Chen, W.; Li, J. T.; Wang, Z.; McHugh, E. A.; Algozeeb, W. A.; Yakobson, B. I.; Tour, J. M. Flash Graphene Morphologies. *ACS Nano* **2020**, *14*, 13691−13699.
(45) Algozeeb, W. A.; Savas, P. E.; Luong, D. X.; Chen, W.; Kittrell, C.; Bhat, M.; Shahsavari, R.; Tour, J. M. Flash Graphene from Plastic Waste. *ACS Nano* **2020**, *14*, 15595−15604.
(46) Solum, M. S.; Sarofim, A. F.; Pugmire, R. J.; Fletcher, T. H.; Zhang, H. ^{13}C NMR Analysis of Soot Produced from Model Compounds and a Coal. *Energy Fuels* **2001**, *15*, 961−971.
(47) Gao, W.; Alemany, L. B.; Ci, L.; Ajayan, P. M. New Insights into the Structure and Reduction of Graphite Oxide. *Nat. Chem.* **2009**, *1*, 403−408.
(48) Yang, Z.; Sun, Y.; Alemany, L. B.; Narayanan, T. N.; Billups, W. E. Birch Reduction of Graphite. Edge and Interior Functionalization by Hydrogen. *J. Am. Chem. Soc.* **2012**, *134*, 18689−18694.
(49) Pugmire, R. J.; Solum, M. S.; Jiang, Y. J.; Sarofim, A. F.; Veranth, J.; Schobert, H. H.; Pappano, P. J. The Study of Soot Formation by Solid State NMR Spectroscopy. *Fuel Chem. Div. Preprints* **2002**, *47*, 733−735.
(50) Jiang, Y. J.; Solum, M. S.; Pugmire, R. J.; Grant, D. M.; Schobert, H. H.; Pappano, P. J. A New Method for Measuring the Graphite Content of Anthracite Coals and Soots. *Energy Fuels* **2002**, *16*, 1296−1300.
(51) Chen, X.; Xu, Z.-H.; Li, X.; Shaibat, M. A.; Ishii, Y.; Ruoff, R. S. Structural and Mechanical Characterization of Platelet Graphite Nanofibers. *Carbon* **2007**, *45*, 416−423.
(52) Vieira, M. A.; Gonçalves, G. R.; Cipriano, D. F.; Schettino, M. A., Jr.; Filho, E. A. S.; Cunha, A. G.; Emmerich, F. G.; Freitas, J. C. C. Synthesis of Graphite Oxide from Milled Graphite Studied by Solid-State ^{13}C Nuclear Magnetic Resonance. *Carbon* **2016**, *98*, 496−503.
(53) Orendt, A. M.; Facelli, J. C.; Bai, S.; Rai, A.; Gossett, M.; Scott, L. T.; Boerio-Goates, J.; Pugmire, R. J.; Grant, D. M. Carbon-13 Shift Tensors in Polycyclic Aromatic Compounds. 8. A Low-Temperature NMR Study of Coronene and Corannulene. *J. Phys. Chem. A* **2000**, *104*, 149−155.

https://doi.org/10.1021/acsnano.1c03197
ACS Nano 2021, 15, 10542−10552

(54) Özcan, N.; Vähäkangas, J.; Lantto, P.; Vaara, J. Characteristic Spectral Patterns in the Carbon-13 Nuclear Magnetic Resonance Spectra of Hexagonal and Crenellated Graphene Fragments. *ChemPhysChem* **2014**, *15*, 1799−1808.
(55) Harris, K. J.; Reeve, Z. E. M.; Wang, D.; Li, X.; Sun, X.; Goward, G. R. Electrochemical Changes in Lithium-Battery Electrodes Studied Using ^{7}Li NMR and Enhanced ^{13}C NMR of Graphene and Graphitic Carbons. *Chem. Mater.* **2015**, *27*, 3299−3305.
(56) Jorio, A.; Cançado, L. G. Raman Spectroscopy of Twisted Bilayer Graphene. *Solid State Commun.* **2013**, *175−176*, 3−12.
(57) Carozo, V.; Almeida, C. M.; Ferreira, E. H. M.; Cançado, L. G.; Achete, C. A.; Jorio, A. Raman Signature of Graphene Superlattices. *Nano Lett.* **2011**, *11*, 4527−4534.
(58) Krauss, B.; Nemes-Incze, P.; Skakalova, V.; Biro, L. P.; Klitzing von, K.; Smet, J. H. Raman Scattering at Pure Graphene Zigzag Edges. *Nano Lett.* **2010**, *10*, 4544−4548.
(59) Nika, D. L.; Balandin, A. A. Two-Dimensional Phonon Transport in Graphene. *J. Phys.: Condens. Matter* **2012**, *24*, 233203.
(60) Kun, P.; Kukucska, G.; Dobrik, G.; Koltai, J.; Kürti, J.; Biró, L. P.; Tapasztó, L.; Nemes-Incze, P. Large Intravalley Scattering Due to Pseudo-Magnetic Fields in Crumpled Graphene. *npj 2D Mater. Appl.* **2019**, *3*, 1−7.
(61) Tkachov, G.; Hentschel, M. Diffusion on Edges of Insulating Graphene with Intravalley and Intervalley Scattering. *Phys. Rev. B: Condens. Matter Mater. Phys.* **2012**, *86*, 205414.
(62) Griffith, D. W. T.; Deutscher, N. M.; Caldow, C.; Kettlewell, G.; Riggenbach, M.; Hammer, S. A Fourier Transform Infrared Trace Gas and Isotope Analyser for Atmospheric Applications. *Atmos. Meas. Tech.* **2012**, *5*, 2481−2498.
(63) Xu, B.; Hirsch, A.; Kronik, L.; Poduska, K. Vibrational Properties of Isotopically Enriched Materials: The Case of Calcite. *RSC Adv.* **2018**, *8*, 33985−33992.
(64) Panich, A. M.; Shames, A. I.; Tsindlekht, M. I.; Osipov, V. Y.; Patel, M.; Savaram, K.; He, H. Structure and Magnetic Properties of Pristine and Fe-Doped Micro- and Nanographenes. *J. Phys. Chem. C* **2016**, *120*, 3042−3053.
(65) Alemany, L. B.; Verma, M.; Billups, W. E.; Wellington, S. L.; Shammai, M. Solid- and Solution-State Nuclear Magnetic Resonance Analyses of Ecuadorian Asphaltenes: Quantitative Solid-State Aromaticity Determination Supporting the Island Structural Model. Aliphatic Structural Information from Solution-State 1H-13C Heteronuclear Single-Quantum Coherence Experiments. *Energy Fuels* **2015**, *29*, 6317−6329.

https://doi.org/10.1021/acsnano.1c03197
ACS Nano 2021, 15, 10542−10552